Research Article

Deep Learning-Based Magnetic Resonance Imaging Image Feature Analysis for Pathological Classification of Brain Glioma

Wei Yao [ID]¹ **and Stefanie Thomas** [ID]²

¹*Department of Radiotherapy, Hunan Cancer Hospital, Changsha 410000, Hunan, China*
²*Department of Computer Science and Automatics, University of Arizona, Tucson 85721, AZ, USA*

Correspondence should be addressed to Wei Yao; yaowei@hnca.org.cn

To explore the application value of MRI in the diagnosis of brain glioma (BG), in the study, a deep learning-based multimodal feature fusion model was established, which was then applied in BG classification. 60 BG patients who came to our hospital for treatment were selected as research subjects. They all accepted the MRI scan and the enhanced scan, and the MRI results were compared with the pathological results. The results showed that the sensitivity of the algorithm was above 90%, and the sensitivity to diagnose grade IV glioma was as high as 98.28%; the specificity was above 78%, and the specificity to diagnose grade IV glioma was as high as 95.85%; the detection accuracy was above 95%. The relative fractional anisotropy (rFA) values of the tumor body were smaller than those of peritumoral edema in both the high-grade group and low-grade group, and the difference was notable ($P < 0.05$); the relative apparent diffusion coefficients (rADC) values of the peritumoral edema were greater than those of tumor bodies of the same grade in both the high-grade group and the low-grade group, and the difference was notable ($P < 0.05$); notable differences were noted in the rADC values of tumor bodies between the high-grade group and the low-grade group ($P < 0.05$) and in the rADC values of the glioma peritumoral edema between the high-grade group and the low-grade group ($P < 0.05$). In summary, MRI based on deep learning raises the sensitivity, specificity, and accuracy to diagnose BG and can more accurately classify BG pathologically, providing reference for clinical treatment of BG.

1. Introduction

Tumor is a disease occurring in multiple sites, and the intracranial tumor is a common disease in the nervous system, which is very harmful to the human nervous system [1]. The intracranial tumor is generally divided into two categories: primary and secondary intracranial tumor. Brain glioma (BG) originates from glial cells and is the most common brain tumor. It is characterized by infiltrating growth, especially high-grade BG [2]. As a result, it is difficult to distinguish it from normal brain tissue, leading to a great risk for surgical resection. Hence, the correct diagnosis and grading of BG before surgery are of great significance for formulating the clinical treatment plan [3, 4]. The tumor grade refers to the degree of malignancy [5]. BGs of grade I and II are of low grade, and those of grades III and IV are of high grade [6].

MRI technology and scanning sequences emerge in endlessly, thanks to the advancement of medical technology and testing equipment. The MRI combines the advantages of anatomy, function, and imaging. It is of great significance for exploring the laws of tumors at the cellular or molecular level and the research and development of drugs, as well as the formation of modern medical modalities and the improvement of human health. Therefore, it is extensively used clinically [7]. To facilitate doctors accurately removing brain gliomas during surgery, imaging methods such as computed tomography (CT), MRI, and positron emission computed tomography (PET) are usually used to segment the glioma area in clinical treatment. Because MRI demonstrates superb capabilities in soft tissue detection and can provide rich

physiological tissue information, it is usually used for preoperative diagnosis, intraoperative treatment, and postoperative examination of BG [8]. The current single-modal MRI technology has its limitations, because it cannot fully display the structure and function of the tumor. The deep learning can automatically learn multilayer features, suitable for auxiliary diagnosis of medical images [9]. In the study, the multimodal MRI technology based on deep learning theory was used to comprehensively display the structure, function, and molecular information of BG, so as to provide diagnostic evidence and reference for the pathological classification of BG.

In summary, the BG patients were selected as the research subjects, and their MRI images were optimized based on deep learning, to evaluate the role of MRI images in classifying BG.

2. Materials and Methods

2.1. Research Subjects and Grouping. 60 BG patients who were admitted to hospital from July 20, 2019, to February 20, 2020, were selected as the research subjects. All patients underwent MRI scan and enhanced scan before surgery, the results of which were compared with postoperative pathological results. According to the pathological classification, they were divided into low-grade BG group (low-grade group) and high-grade BG group (high-grade group). There were 44 males and 16 females between 20 and 60 years of age, and the average age was 55.82 ± 4.18 years. The study has been approved by medical ethics committee of Hunan Cancer Hospital, and the patients and their families have been informed and signed the consent form.

The MRI diagnostic criteria strictly followed the 2015 edition of the Guidelines for the Diagnosis and Treatment of Glioma of the Central Nervous System in China [10]. MRI imaging features of low-grade BG are as follows: uniform signal, long T_1, and long T_2. Enhanced scans showed that there was no diffuse astrocytoma. When the signal was uneven and locally accompanied by massive calcification, it was considered oligodendrocytes cell tumor. Grade III glioma is also called gradual glioma. Its MRI signal characteristics were the same as low-grade glioma, but the enhanced scan showed that there was enhancement. Grade IV glioma exhibited irregular peripheral enhancement, accompanied by a large amount of central necrosis and obvious brain edema outside the enhanced area. The enhancement scan of glioma sarcoma exhibited solid uneven enhancement.

For glioma classification, according to the degree of malignancy from low to high, it can be divided into grades I~IV, strictly referring to the 2007 edition of WHO glioma pathological grading standards.

Inclusion criteria are as follows: (1) All cases accepted MRI scan, diagnosed by clinical imaging physicians and neurosurgeons strictly referring to MRI diagnostic criteria. (2) The patients were diagnosed as BG according to postoperative pathological results. (3) The patient had no history of craniocerebral surgery and substantial brain injury. (4)

Patients had clear consciousness, were able to communicate normally, and had no mental illness.

Exclusion criteria are as follows: (1) cases diagnosed as having cerebral infarction by DWI or MRS, (2) cases with severe communication disorder or mental illness, (3) cases with intracranial hypertension and other characteristics of intracranial lesions, and (4) patients with liver and kidney dysfunction or allergy to contrast agents.

2.2. MRI Examination. After routine preparations, all patients were asked to lie on their backs, headfirst, with their upper limbs placed on both sides of the body. Special earplugs were inserted into the ear, and the patients were told not to move [11]. The equipment used was GE Signa HD 3.0 T magnetic resonance whole-body scanner (Schering, Germany). After conventional axial, sagittal, and coronal scans, axial and sagittal T1FLAIR scans were performed again immediately after the contrast agent was injected. If necessary, coronal enhancement scan was required. The enhanced scanning adopted MRI special high-pressure injector. After the paramagnetic contrast agent was injected into the anterior elbow vein at a dose of 0.1 mmoL/kg body weight, 15 mL of normal saline was injected immediately, so that the contrast agent can be fully distributed into the patient's body. The thickness of scanning layer was about 5 mm, the layer distance was 1.5 mm, and the number of layers was 20.

After reading the patient's medical history and MRI imaging results, two radiologists observed and analyzed the patient's images to determine the BG classification. Any inconsistency was resolved through discussion. Based on postoperative pathological diagnosis, the image features of BG of different pathological grades were compared and analyzed.

2.3. Pathological Examination. The specimen was fixed in 10% neutral formalin, embedded in paraffin, and sliced continuously in $4 \mu m$ thickness. After being stained using HE staining, it was visualized and observed by the senior physician according to the 2007 edition of the WHO International Classification of Brain Tumors [12], with the pathological grade and grouping determined: low-grade BG group, mainly for patients with grade I and grade II BG, and high-grade BG group, mainly for patients with grade III and grade IV BG.

2.4. The Deep Learning Model Based on Multimodal Feature Fusion. At present, convolutional neural networks are widely used in the field of medical image diagnosis, with good progress achieved. The working mechanism of convolutional neural network is to automatically extract image features through convolution operation, with rich semantic information and strong robustness [13]. Since the deep learning model can obtain better results through training labeled images, the second to fifth convolution blocks of VGG16 [14] are directly applied in transfer learning. The feature map of the last layer of each

convolution block is extracted and processed, which is $K(g)$, $g = 1, 2, 3, 4, 5$, respectively. After upsampling, $K(g)$ and $K(g-1)$ fuse the pixel using the result image processed by $2*3$ convolution kernel, and then the $6*6$ convolution kernel is used again to correct the fused image, which can eliminate the aliasing effect and obtain a new feature map $K(g-1)$. The pyramid fusion equation is as follows:

$$K(g-1) = R_{2\times3}(K(g-1)),$$
$$K(g-1) = R_{6\times6}(K(g) + K(g-1)). \tag{1}$$

$K(3)$ in the last layer passes through the Batch Normal (BN) layer, the adaptive maximum pooling layer, and the fully connected layer in turn. The BN layer can speed up the convergence speed and improve classification effect of the model. $R^{(1)}$ is set as the n-th dimension feature of $K(3)$. $R^{(1)}$ introduces the parameters $L^{(1)}$ and $T^{(1)}$ and uses the indifference estimation to output the n-th dimension feature as follows:

$$R^{(1)} = L^{(1)}\bar{P}^{(1)} + T^{(1)}. \tag{2}$$

When nonlinear factors are added to the ReLU layer, the expression ability of the increased model will be weakened. The activation function of ReLU is as follows. $Q(\cdot)$ is the expression ability of the nonlinear model, and x is the maximum solution.

$$Q(x) = \max\{0, x\}. \tag{3}$$

The main difference between the adaptive maximum pooling layer and the standard Max Pooling is that the former will control the output-size (Out) according to the input-size (In), and stride and kernel size are expressed as follows:

$$\text{stride} = \text{floor}\left(\frac{\text{In}}{\text{Out}}\right),$$
$$\text{kernelsize} = \text{In} - (\text{Out} - 1) \times \text{stride}. \tag{4}$$

The fully connected layer can be regarded as a full-scale convolution of $s \times u$, with s and u being the output size of the previous layer. Finally, 1026-dimensional features extracted by the convolutional neural network can be obtained.

$$k = (k_1, k_2, k_3 L k_{1026}). \tag{5}$$

The functions of different modes have different characteristics [15]. In the study, a deep learning model of multimodal feature fusion is established. The model contains less neurons versus the hidden planes and Sigmoid layers. The entire network is trained by maximizing the energy proportion of the feature layer. The Sigmoid layer can map the feature interval after feature fusion. The feature interval is $(0, 1)$, which is the prediction probability. The feature vector $f = (1, 0)$, and the forward propagation equation is as follows:

$$V_f = (W_i + N_i)\gamma_{ie} + \wp_e,$$
$$N = \wp\left(\sum_{s=1}^{m}(W_i + N_i)\wp_{ie} + \gamma_e\right), \tag{6}$$

where $V(f) = (1/1 + e^{-i})$, W_i is the deviation of the visible layer, γ_e is the deviation of the hidden layer, and $\wp_{ie}$ is the hidden layer vector. To obtain the optimal fitting multimodal feature, the energy model is used to adjust the parameters, and the energy function is as follows:

$$K(1, 0|\nabla) = -\sum_{e=1}^{i} W_e N_e - \sum_{s=1}^{m}\sum_{i=1}^{e} W_i \wp_{ie} N_i. \tag{7}$$

In equation (9), $\nabla = (W_i, \wp_{ie}, N_i)$, $K(1, 0|\nabla)$ represents the total energy of the module.

The marginal probability distribution is defined as follows:

$$g(1|\nabla) = \frac{1}{J(\nabla)}\sum_e O^{-k(1,0|\nabla)}, \tag{8}$$

$$g(0|\nabla) = \frac{1}{J(\nabla)}\sum_i o^{-k(1,0|\nabla)}, \tag{9}$$

where $g(\nabla) = \sum_{il} O^{-k(1,0|\nabla)}$ is the optimized nonlinear function expression.

$$\nabla_{il} = \arg\max_{\nabla}\sum_{i=1}^{o} lgg(1_i|\nabla), \tag{10}$$

where o is the number of samples. When ∇ reaches the maximum, the energy of the hidden layer is the smallest. When data is transmitted within the network, the direction of the data flow is also the direction of energy dissipation. After multiple iterations, the network energy is gradually attenuated, and the network tends to be orderly or the probability distribution tends to be concentrated.

2.5. Evaluation Indicators. Accuracy, sensitivity, and specificity were used to quantitatively evaluate the performance of the model. The main observation indicators of the lesion image included the location of the lesion, the number of lesions, the size of the lesion, the shape of the lesion, the signal intensity, the edema around the tumor, and the degree of enhancement [16]. After the original MRI image was transmitted to the workstation, it was processed by the Function tool (2) software to obtain the ADC map and FA map, with the FA value and ADC value measured. Subsequently, the rFA and rADC values were obtained according to the ratio of the tumor body part and the tumor edema zone to the contralateral white matter area, respectively.

2.6. Statistical Methods. The data was processed using SPSS19.0 statistical software. The measurement data were expressed as mean ± standard deviation ($\bar{x} \pm s$). The comparison of the mean between each group was performed by t-test. The count data were expressed by percentage (%), and

the χ^2 test was used. $P < 0.05$ was the threshold for significance.

3. Results

3.1. The General Information. The 60 BG patients included were 44 males and 16 females (Figure 1). 23 cases were in the low-grade BG group, 13 were males, and 10 were females, with an average age of 54.16 ± 3.45 years. 37 cases were in the high-grade BG group, and there were 20 males and 17 females, with an average age of 53.45 ± 4.18 years (Figure 2). There was no notable difference in general information between the two groups of patients ($P > 0.05$), and they were comparable between groups.

3.2. The Pathological Results. According to the WHO international classification and grading standards, all patients were divided into high-grade BG group and low-grade BG group. Pathological examination showed that there were 23 cases in low-grade BG group: 6 cases of grade I astrocytoma and 17 cases of secondary cell tumor. There were 37 cases in high-grade BG group: 7 cases of grade III anaplastic oligodendroglioma, 10 cases of grade III anaplastic astrocytoma, and 20 cases of grade IV glioblastoma (Figure 3).

3.3. Diagnosis of BG Based on Deep Learning Algorithms. According to Figure 4, it was evident that, after fusion with traditional features and deep learning features, MRI has seen improvement in various indicators to a certain extent. The sensitivity of the algorithm was above 90%, and the sensitivity to diagnose grade IV glioma was as high as 98.28%; the specificity was above 78%, and the specificity to diagnose grade IV glioma was as high as 95.85%; the detection accuracy was above 95%. This showed that MRI based on the deep learning had relatively good performance in detecting BG, and it can be used for clinical diagnosis of BG, assisting physicians in diagnosing high-risk patients.

3.4. MRI Image Analysis. Figure 5 was an MRI image showing intracranial abscess foci and tumor necrosis. Obviously, the number of cells and high viscosity in the abscess focus restricted the diffusion and movement of water molecules.

Figure 6 was the MRI image of a female with BG, aged 44. It was evident that the decrease in the extracellular space and the increase in the ratio of nucleus to cytoplasm led to diffusion limitation of water molecule of high-grade tumor. Correspondingly, the ADC value was negatively correlated with tumor grade, and tumors of a lower grade often had higher ADC values.

Figure 7 was the MRI image of a male with BG, aged 45. It was evident that the rCBV in the high-grade group was higher compared to that in the low-grade group.

3.5. Comparison of rFA. It was evident from Figure 8 that the rFA values of tumor bodies in the high-grade and low-grade
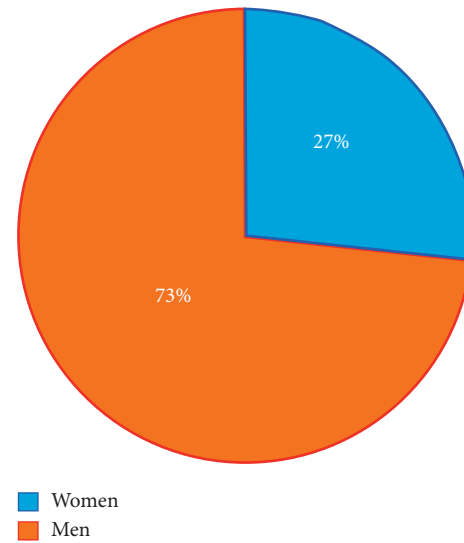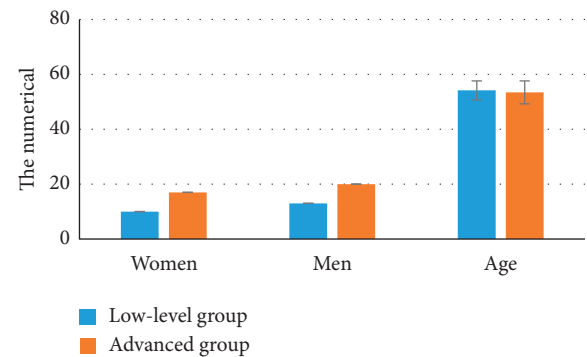

FIGURE 1: The ratio of males to females.

FIGURE 2: The general information.

groups were 0.3192 and 0.3771, respectively, both smaller than the rFA values of peritumoral edema ($P < 0.05$).

3.6. Comparison of rADC. Figure 9 shows the rADC values between the high-grade group and the low-grade group. The rADC values of the peritumoral edema in the high-grade group and the low-grade group were 1.482 and 2.082, respectively, both greater than the rADC values of tumor bodies of the same grade ($P < 0.05$). The rADC values of the tumor bodies in the high-grade group and the low-grade group were 1.853 and 1.352, respectively ($P < 0.05$). Notable differences were noted in the rADC values of the peritumoral edema between the high-grade and low-grade groups ($P < 0.05$).

4. Discussion

BG is a common intracranial tumor. To formulate the best treatment plan and evaluate the prognosis, it is necessary to accurately classify the BG. Pathological biopsy is a common method used to classify BG, but it is sometimes not accurate enough, because BG can be heterogeneous, and the same tumor may have pathological features of two or more grades
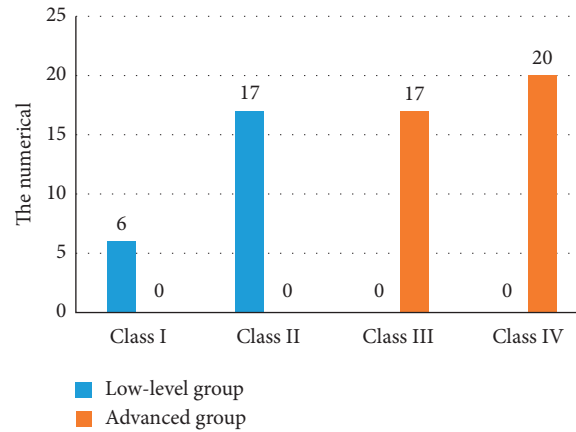
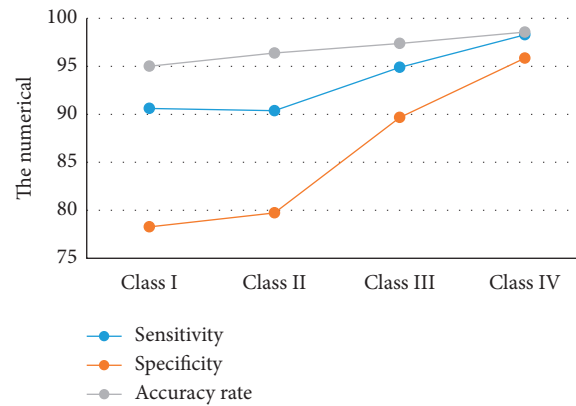FIGURE 3: Pathological classification of patients.

FIGURE 4: Performance of deep learning algorithms.

at the same time. MRI technology assists in the preoperative grading of glioma, which is of great significance for formulating the proper diagnosis and treatment plan of BG. In the study, a deep learning-based multimodal feature fusion model was established, which was then applied in BG classification. The results found that, after combination with traditional features and deep learning features, the MRI has seen improvement in various indicators to a certain extent. The sensitivity of the modified algorithm was above 90%, and the sensitivity to diagnose grade IV glioma was as high as 98.28%. The specificity was above 78%, and the specificity to diagnose grade IV glioma was as high as 95.85%. The accuracy was above 95%. This illustrated that the MRI based on the deep learning model had relatively good performance in detecting BG, and it can be used for clinical diagnosis of BG, assisting physicians in diagnosing high-risk patients. The research results were similar to those of Kocher et al. (2020) [17], and both show that the optimized deep learning algorithm applied to MRI image diagnosis can improve the sensitivity and accuracy of diagnosis.

The ADC value reflects the average value of the diffusion of water molecules in the body in all directions. It is used to express the speed and range of the diffusion movement of water molecules in the patient's body. If the diffusion of water molecules is more obvious, the ADC value is higher. The tumor cell infiltration and edema, resulting from canceration, will change the diffusion ability of water molecule in the local brain tissue, leading to changes in ADC values. In the experiment, the rADC values of the peritumoral edema zone of the high-grade group and the low-grade group were both greater than that of the tumor of the same grade, and the difference was notable ($P < 0.05$). A notable difference was noted in the rADC value between the high-grade group and the low-grade group ($P < 0.05$) and the rADC value of the glioma peritumoral edema zone between the high-grade group and the low-grade group ($P < 0.05$). This was in line with the conclusion of Volovitz et al. that the rADC value of the tumor area and the contralateral normal white matter area showed a negative correlation with the tumor grade. This is due to the infiltration and growth of gliomas. Because the pathological grade, tumor size, location, and cell composition are different, the infiltration of tumor cells to surrounding fibers is also distinct. Notable differences were noted between the rFA values of tumor bodies with the rFA values of peritumoral edema zones in both the high-grade and low-grade groups ($P < 0.05$). The FA value can be used to distinguish normal tissue from
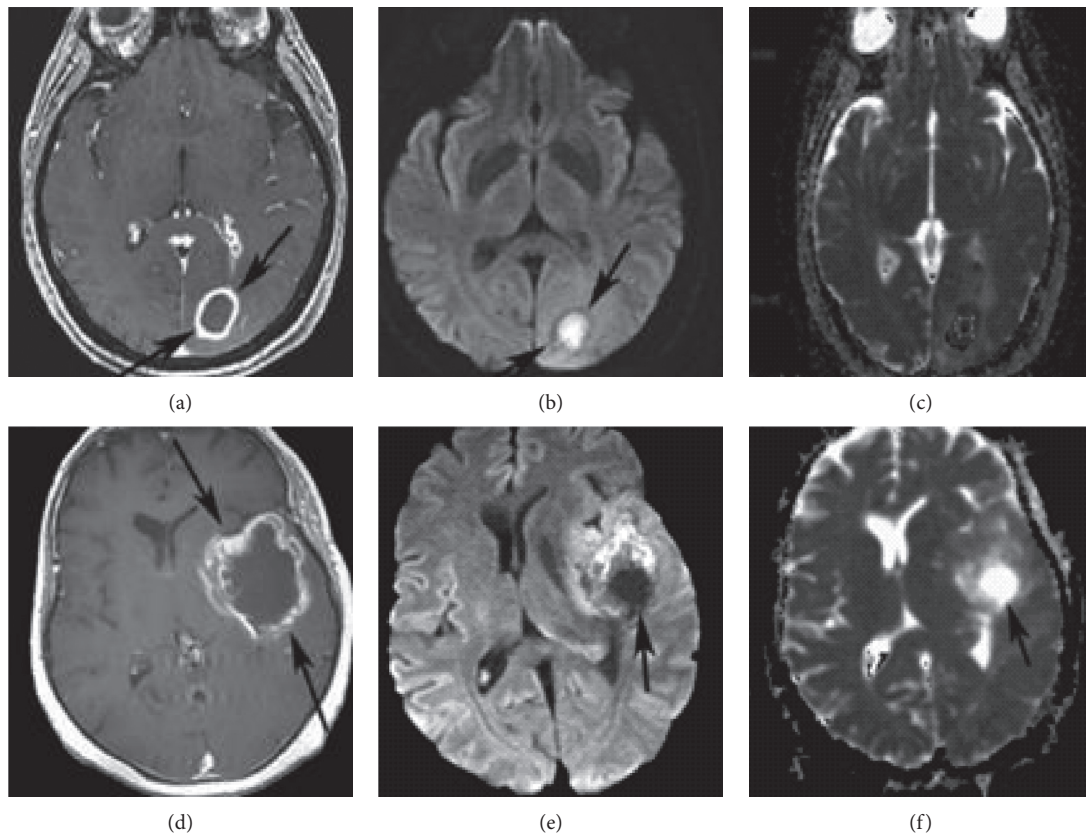
(a) (b) (c)

(d) (e) (f)

Figure 5: An MRI image of intracranial abscess foci accompanied by tumor necrosis. The abscess focus of the left occipital lobe showed circular T1 enhanced signals (a), DWI high signal (b), and ADC low signal (c). The glioblastoma in the left insular lobe showed irregular T_1 circular enhancement (d), low DWI signal (e), and high ADC signal (f).
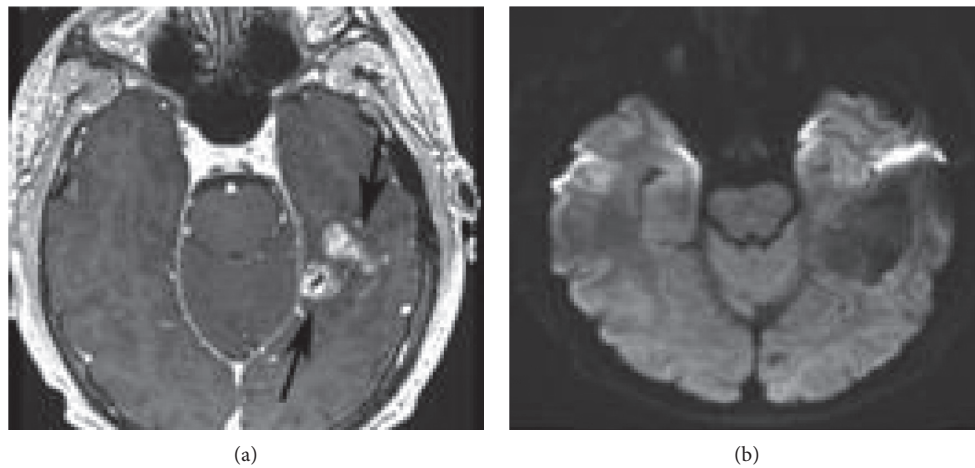
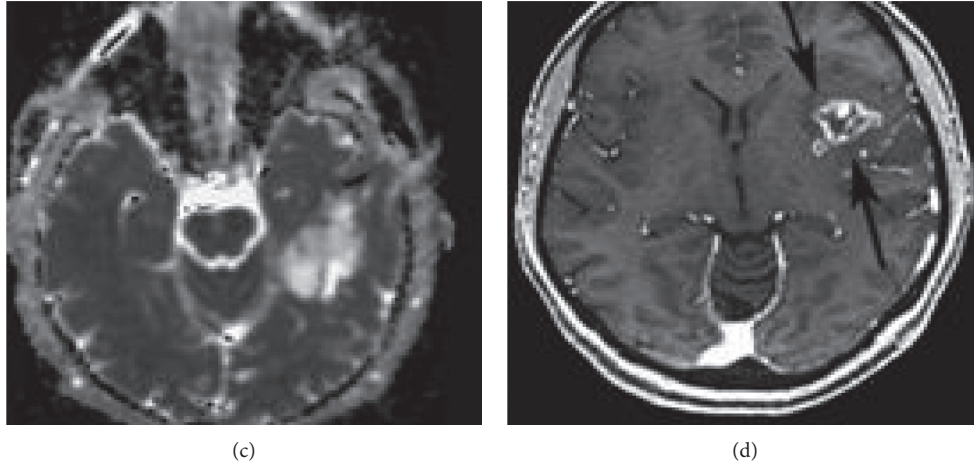

(a) (b)

Figure 6: Continued.

(c)

(d)

FIGURE 6: An MRI image of a female with BG. Low-grade astrocytoma of the left temporal lobe showed uneven enhancement for T1WI (a), low signal for DWI (b), and high signal for ADC (c). The glioblastoma on the left insular lobe showed uneven enhancement for T1WI (d).
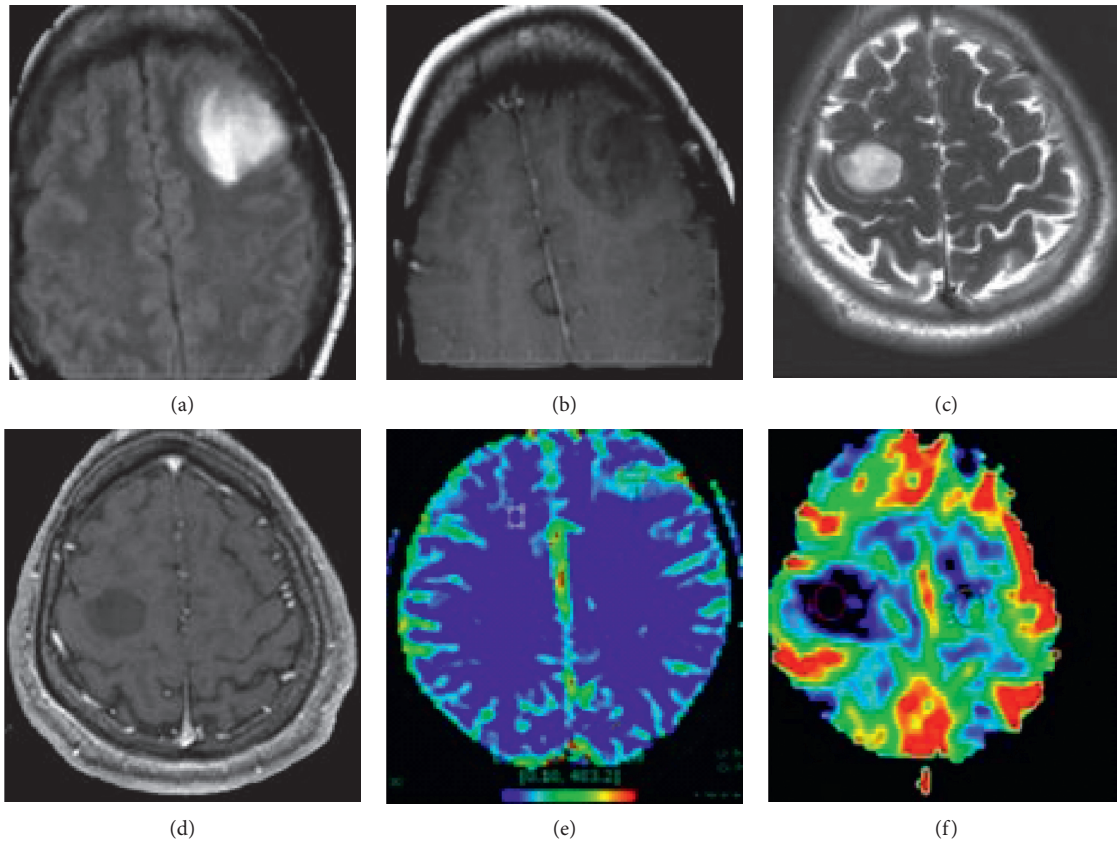

(a)

(b)

(c)

(d)

(e)

(f)

FIGURE 7: An MRI image of a male with BG. FLAIR sequence of patients with grade III anaplastic astrocytoma (a) indicated a hyperintensity focus in the left frontal lobe and a hypointensity for TIWI enhancement (b). There was no enhancement due to the integrity of the blood brain barrier. The CBV value on the left side of the rCBV was 5.7 times higher than that of the contralateral frontal lobe, indicating that the tumor tissue had a higher capillary density (c); in patients with grade II fibrous astrocytoma, a hyperintensity focus was observed in the right frontal lobe for T2WI (d). Similarly, there was no obvious enhancement for the focus (e), and there was no obvious increase in focal rCBV (f).

tumor enhancement areas, necrotic cystic areas, and peritumoral edema zones. Nalawade et al. (2019) [18] believed that FA values can distinguish high-grade and low-grade gliomas, and they were instrumental in classification of BG. In this study, the rFA values of the tumor body were notably different from those of peritumoral edema zone in both the high-grade group and the low-grade group, indicating that the rFA value can be
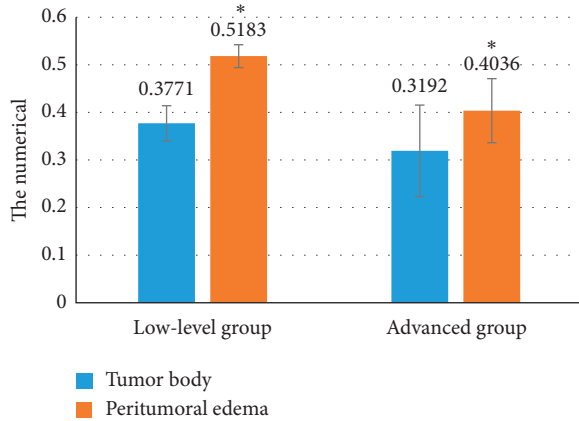
FIGURE 8: Comparison of rFA values. ∗ indicates that the rFA values of the tumor body were notably different from the rFA values of peritumoral edema of the same grade in both the high-grade and low-grade groups ($P < 0.05$).
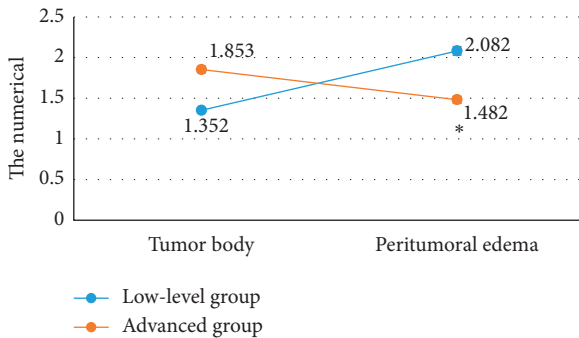

FIGURE 9: Comparison of rADC values between the two groups. ∗ indicates that the rADC value of tumor body was notably different from the rADC value of peritumoral edema of the same grade in both the low-grade group and the high-grade group ($P < 0.05$).

used to distinguish the tumor body from the peritumoral edema zone. However, the sample size is small, which may reduce the power of the results in the study.

5. Conclusion

In the study, a deep learning-based multimodal feature fusion model was established, which was then applied in BG classification. It was found that MRI based on deep learning evidently improved the classification results of glial tumors, showing increased sensitivity, specificity, and accuracy. However, some limitations should be noted. The sample size is small, which will reduce the power of the study. In the follow-up, an expanded sample size is necessary to strengthen the findings of the study. MRI based on deep learning raises the sensitivity, specificity, and accuracy to diagnose BG and can more accurately classify BG pathologically, providing reference for clinical treatment of BG.

Data Availability

No data were used to support this study.

Conflicts of Interest

The authors declare that they have no conflicts of interest.

References

[1] S. Perreault, V. Larouche, U. Tabori et al., "A phase 2 study of trametinib for patients with pediatric glioma or plexiform neurofibroma with refractory tumor and activation of the MAPK/ERK pathway: TRAM-01," *BMC Cancer*, vol. 19, no. 1, p. 1250, 2019.

[2] J. Bai, J. Varghese, and R. Jain, "Adult glioma WHO classification update, genomics, and imaging: what the radiologists need to know," *Topics in Magnetic Resonance Imaging*, vol. 29, no. 2, pp. 71–82, 2020.

[3] S. J. Price and J. H. Gillard, "Imaging biomarkers of brain tumour margin and tumour invasion," *The British Journal of Radiology*, vol. 84, no. 2, pp. S159–S167, 2011.

[4] R. J. Slegers and I. Blumcke, "Low-grade developmental and epilepsy associated brain tumors: a critical update 2020," *Acta Neuropathologica Communications*, vol. 8, no. 1, p. 27, 2020.

[5] H. Backes, R. Ullrich, B. Neumaier, L. Kracht, K. Wienhard, and A. H. Jacobs, "Noninvasive quantification of 18F-FLT human brain PET for the assessment of tumour proliferation in patients with high-grade glioma," *European Journal of Nuclear Medicine and Molecular Imaging*, vol. 36, no. 12, pp. 1960–1967, 2009.

[6] I. J. Abecassis, B. Cordy, S. Durfy et al., "Evaluating angioarchitectural characteristics of glial and metastatic brain tumors with conventional magnetic resonance imaging," *Journal of Clinical Neuroscience*, vol. 76, pp. 46–52, 2020.

[7] B. R. J. van Dijken, P. J. van Laar, G. A. Holtman, and A. van der Hoorn, "Diagnostic accuracy of magnetic resonance imaging techniques for treatment response evaluation in patients with high-grade glioma, a systematic review and meta-analysis," *European Radiology*, vol. 27, no. 10, pp. 4129–4144, 2017.

[8] C. W. Shen, J. T. Ho, P. Ly et al., "Behavioural intentions of using virtual reality in learning: perspectives of acceptance of information technology and learning style," *Virtual Reality*, vol. 23, no. 3, pp. 313–324, 2018.

[9] Z. Lv and W. Xiu, "Interaction of edge-cloud computing based on SDN and NFV for next generation IoT," *IEEE Internet of Things Journal*, vol. 7, no. 7, pp. 5706–5712, 2020.

[10] I. Volovitz, N. Shapira, H. Ezer et al., "A non-aggressive, highly efficient, enzymatic method for dissociation of human brain-tumors and brain-tissues to viable single-cells," *BMC Neuroscience*, vol. 17, no. 1, p. 30, 2016.

[11] A. Vamvakas, S. C. Williams, K. Theodorou et al., "Imaging biomarker analysis of advanced multiparametric MRI for glioma grading," *Physica Medica*, vol. 60, pp. 188–198, 2019.

[12] S. D. Sasi, Ramaniharan, K. Anandh et al., "Evaluating feasibility of high resolution T_1-perfusion MRI with whole brain coverage using compressed SENSE: application to glioma grading," *European Journal of Radiology*, vol. 129, p. 109049, 2020.

[13] K. Aslan, H. P. Gunbey, L. Tomak, and L. Incesu, "Multiparametric MRI in differentiating solitary brain metastasis from high-grade glioma: diagnostic value of the combined use of diffusion-weighted imaging, dynamic susceptibility contrast imaging, and magnetic resonance spectroscopy parameters," *Neurologia i Neurochirurgia Polska*, vol. 53, no. 3, pp. 227–237, 2019.

[14] M. Shaver, P. Kohanteb, C. Chiou et al., "Optimizing neuro-oncology imaging: a review of deep learning approaches for glioma imaging," *Cancers*, vol. 11, no. 6, p. 829, 2019.

[15] K. Chang, A. L. Beers, H. X. Bai et al., "Automatic assessment of glioma burden: a deep learning algorithm for fully automated volumetric and bidimensional measurement," *Neuro-Oncology*, vol. 21, no. 11, pp. 1412–1422, 2019.

[16] C. G. Bangalore Yogananda, B. R. Shah, M. Vejdani-Jahromi et al., "A novel fully automated MRI-based deep-learning method for classification of IDH mutation status in brain gliomas," *Neuro-Oncology*, vol. 22, no. 3, pp. 402–411, 2020.

[17] M. Kocher, M. I. Ruge, N. Galldiks, and P. Lohmann, "Applications of radiomics and machine learning for radiotherapy of malignant brain tumors," *Strahlentherapie und Onkologie*, vol. 196, no. 10, pp. 856–867, 2020.

[18] S. Nalawade, G. K. Murugesan, M. Vejdani-Jahromi et al., "Classification of brain tumor isocitrate dehydrogenase status using MRI and deep learning," *Journal of Medical Imaging*, vol. 6, no. 4, p. 046003, 2019.